

Full Length Article

Novel soot loading prediction model of diesel particulate filter based on collection mechanism and equivalent permeability

De-yuan Wang^a, Pi-qiang Tan^{a,*}, Lei Zhu^b, Yin-huan Wang^b, Zhi-yuan Hu^a, Di-ming Lou^a

^a School of Automotive Studies, Tongji University, Shanghai 201804, PR China

^b Kailong High Technology Company Limited, Wuxi 214000, PR China

ARTICLE INFO

Keywords:

Diesel engine

DPF

Soot loading

Prediction

Collection mechanism

ABSTRACT

Accurate estimation of soot loading in DPF is an important basis for the efficient application of diesel exhaust aftertreatment system. However, some prediction methods need to be equipped with additional equipment, which increases the cost and does not significantly improve the accuracy of soot loading prediction. Moreover, the previous soot loading prediction models rarely consider the ash deposition and particle collection rules from the perspective of collection mechanism. In this study, a novel soot loading prediction model based on collection mechanism and multilayer equivalent permeability considering the deep bed and filter cake collection stage is proposed. The prediction model is based on theory of packed beds of spherical particles. The wall and cake are divided into four different layers: particulate layer, ash layer, wall layer, and clean wall layer, respectively. Finally, the overall soot loading equation is established and the numerical solution is solved by Taylor's formula. The model is verified by bench test, which can ensure high prediction accuracy without increasing the cost of regeneration. The maximum prediction error is less than 5%, and the average error is 2.72%. Based on the model, effects of the key structural parameters such as DPF diameter, length, cell density and wall thickness, as well as the engine operating parameters such as exhaust mass flow and temperature on the pressure drop and soot loading characteristics were further researched. The research results can provide important guidance for accurate triggering of regeneration, formulation of active regeneration control strategy and improvement of DPF durability.

1. Introduction

Diesel engines have the advantages of good durability, high thermal efficiency, and low fuel consumption [1–3], which are widely used in mobile and stationary applications [1]. However, the in-cylinder diffusion combustion of diesel engine causes serious particulate matter (PM) pollution [4,5].

Diesel PM can be classified into three modes: nucleation, accumulation, and coarse, whose number and size distribution shows bimodal patterns [6,7]. Diesel PM is composed of soot, soluble organic fraction (SOF), ash, sulfate, and other substances [4]. Diesel PM formation mainly occurs in the process of pyrolysis, nucleation, surface growth, coalescence, agglomeration, and oxidation [8]. Furthermore, PM is generally a chain-like or grape-like aggregate composed of primary particles. These primary particles consist of onion-like carbon layers with a distinct core-shell structure [9]. Characteristics of diesel PM are influenced by quality of fuel and lubricating oil [10–12], operating

condition [13], injection strategy [14,15], and exhaust aftertreatment technology [16,17].

More and more stringent regulations are implemented to reduce diesel PM emissions. In-cylinder PM reduction technology cannot enable diesel engine to meet the latest emission limit requirements. Diesel particulate filter (DPF) has been recognized as the most important technology for reducing diesel PM pollutants [3]. Modern DPF is wall-flow honeycomb structure, mainly composed of cordierite or silicon carbide, with high thermochemical stability and low thermal expansion. DPF is generally composed of thousands of square parallel channels. The other end of adjacent channel is blocked. Inlet channel exhaust flows through wall to adjacent outlet channel, so most PM accumulates in the DPF.

With the continuous PM deposition in DPF substrate, the exhaust back pressure continues to rise, which deteriorates the fuel consumption and the power performance of diesel engine. Therefore, active regeneration is required to remove accumulated PM in time. The current

* Corresponding author.

E-mail address: tanpq@hotmail.com (P.-q. Tan).

<https://doi.org/10.1016/j.fuel.2020.119409>

Received 30 July 2020; Received in revised form 23 September 2020; Accepted 3 October 2020

Available online 19 October 2020

0016-2361/© 2020 Elsevier Ltd. All rights reserved.

active regeneration raises the DPF inlet temperature above 550 °C through in-cylinder post injection or tailpipe injection, resulting in quickly burn off of accumulated PM [18]. Starting active regeneration too early or too late can cause problems such as increased fuel consumption or reduced DPF reliability. It is necessary to develop reasonable active regeneration control strategy, whose important basis is the soot loading. However, the phenomena in DPF is complicated, and performing measurements inside DPF is difficult.

An effective method to accurately estimate the soot loading in DPF in real time is to establish DPF models. Bisset's theory based on packed bed of spherical particles [19] as well as Konstandopoulos and Johnson's work [20] has served as a basis for DPF model establishment [21]. Kuwabara's flow field around collector unit has been applied in their research [22,23]. Consistent with experimental evidence, soot can only partially penetrate into the porous wall, [22] which has been already obtained at early DPF development by Murtagh et al. [24] Serrano et al. [22] proposed a collection model to predict the combined response of pressure drop and filtration efficiency, mainly assuming low PM penetration thickness. Payri et al. [21] presented a lumped calculation method where characteristics of porous wall are simplified to a function of soot loading. Uenishi et al. [25] built the relationship between wall porosity and permeability under different soot loading amount. They derived a function of the average diameter of PM aggregates, which can be used in wall porosity prediction. Bollerohoff et al. [26] proposed an advanced collection model, which accounts for filtration characteristic for non-homogeneous substrate structures. In addition, Lizarraga et al. [17], Bensaid et al. [27], Tsujimoto et al. [28], Thompsett et al. [29], Karin et al. [11], Zhang et al. [30], E and Gong [31], Bai et al. [32,33], and many other researchers have performed significant exploration on DPF model establishment. Bai et al. [32] built a new soot loading model to improve the accuracy of regeneration trigger time. It should be noted that the transient PM emission is a function of stable PM emission, stable excess air coefficient, and transient excess air coefficient. Huq et al. [34] presented a sensing method that can measure in situ soot loading using electrical capacitance imaging, offering an effective approach for soot loading measurement. Zhang et al. [35] predicted the ash deposition mass by the fuzzy adaptive variable weight functional link neural network (FAV) model. Endpoints of soot loading with different initial mass and fuels were predicted based on the cusp catastrophe model. Results show that the FAV model has higher prediction accuracy than other single prediction methods, with an average error of 2.24%. Huang et al. [36] developed and experimentally studied an open-loop online method to estimating soot loading based on soot mass balance, through establishing and combining NO_x and soot emission models and passive regeneration model considering the catalytic soot oxidation characteristics. In addition to determining soot load amount through DPF pressure drop, microwave-based methods can also perform direct and in-situ soot loading detection [37]. Feulner et al. [38] compared different soot sensing methods, and found the microwave-based signal can deduce the engine out soot emission by a time derivative, and determine the soot loading through integrating the measured PM mass. Furthermore, Shuai et al. [39], Meng et al. [40], Chen et al. [41], Palma et al. [42], Trandafilovic et al. [43], Rico Perez et al. [44], Rothe et al. [45], Liu et al. [46], and many other researchers have performed significant exploration on DPF ash deposition and soot loading prediction.

In summary, some soot loading prediction methods need to be equipped with additional equipment, which increases the cost and does not significantly improve the prediction accuracy. Moreover, the previous soot loading prediction models rarely consider the ash deposition and particle collection rules from the perspective of collection mechanism. In this study, a novel soot loading prediction model based on collection mechanism and multilayer equivalent permeability is proposed, which can ensure high prediction accuracy without increasing the cost of regeneration. The model has been verified by bench test with high accuracy, and can be used for active injection of tailpipe injection. Based on the model, effects of the key structural parameters such as DPF

diameter, length, cell density and wall thickness, as well as the engine operating parameters such as exhaust mass flow and temperature on DPF pressure drop and soot loading characteristics were studied. The research results can provide important guidance for accurate triggering of regeneration, formulation of active regeneration control strategy and improvement of DPF durability.

2. Establishment of soot loading prediction model

2.1. Model assumptions

Fig. 1 shows the wall-flow structure and wall microstructure [22]. PM penetration only accounts for a small part of wall thickness, usually less than 5% [22,47].

The influence of DPF porous wall on PM collection depends on its microstructure characteristics, such as average pore diameter (d_{pore}) and porosity ($\varepsilon_{DPF,0}$) [20,49,50]. In the theory spherical particle packed bed, the porous wall is considered as multiple groups of cell units, where the collector unit exist. When PM continues to deposit, the diameter of the former remains unchanged, while the diameter of the latter keeps increasing. The main model assumptions are as follows: (i) $\varepsilon_{DPF,0}$ is same as porosity of spherical cell unit (ε_0); (ii) Specific surface area of wall is the same as that of cell unit [20,26,49].

Therefore,

$$\begin{cases} \varepsilon_{DPF,0} = \varepsilon_0 \\ \frac{6(1 - \varepsilon_0)d_{f,0}^2}{d_{f,0}^3} = \frac{k_{pore}\varepsilon_{DPF,0}}{d_{pore,0}} \end{cases} \quad (1)$$

$$d_{f,0} = \frac{6(1 - \varepsilon_0)d_{pore,0}}{k_{pore}\varepsilon_{DPF,0}} \quad (2)$$

where d_f is the diameter of collector unit. k_{pore} is associated with the pore model inside porous substrate. For cylindrical pore model, $k_{pore} = 4$. For flat plate pore model, $k_{pore} = 2$. The pore model is cylindrical in this study. $\varepsilon_{DPF,0}$ is 0.55, and $d_{pore,0}$ is 12 μm . PM is deposited around the collector unit until the cell unit is full of PM [25,26,47]. the subscript 0 means that the DPF is in the initial state. The cell unit diameter (d_{cell}) is expressed as [47,51].

$$d_{cell} = \frac{d_{f,0}}{(1 - \varepsilon_0)^{1/3}} \quad (3)$$

The collector unit diameter ($d_{f,0}$) is given by [25,26,47]

$$d_{f,0} = 1.5 \left(\frac{1 - \varepsilon_w}{\varepsilon_w} \right) d_{pore,0} \quad (4)$$

DPF mainly takes effect by the following two stages: [30,50] (i) Stage of deep bed filtration. It happens in clean DPFs, whose main collection mechanisms are Brown diffusion and interception. (ii) Stage of cake filtration. When the cell unit is full of PM, cake layer is formed on the substrate surface, significantly improving the filtration efficiency [22,50].

Channel cross section and cake and wall structure are shown in Fig. 2. In this study, the wall and cake are divided to four different layers. They are called clean wall layer, wall layer, ash layer, and particulate layer. Their thicknesses are δ_{cw} , δ_{wl} , δ_{al} , and δ_{pl} , respectively.

The relationship between each layer thickness is given by

$$\begin{cases} \delta_{w,DPF} = \delta_{cw} + \delta_{wl} \\ \delta_c = \delta_{al} + \delta_{pl} \end{cases} \quad (5)$$

The cross sectional areas of particulate layer and ash layer are A_{pl} and A_{al} , respectively. The masses of them are m_{al} and m_{pl} . The channel width is $d_{k,DPF}$, and the length of single channel is L_{DPF} . Therefore,

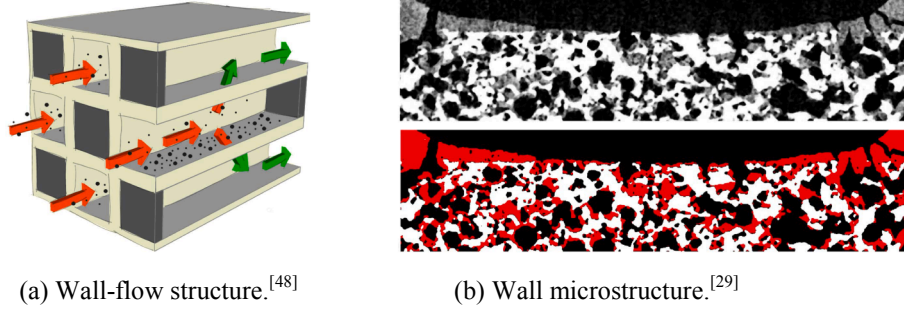


Fig. 1. Wall-flow structure and wall microstructure.

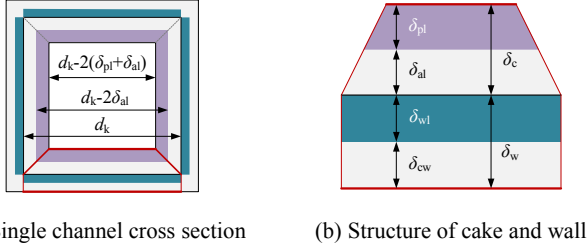


Fig. 2. Channel cross section and cake and wall structure.

$$d_{k,DPF} = \frac{0.0254}{\sqrt{\sigma_{DPF}}} - \delta_{w,DPF} \quad (6)$$

$$\begin{cases} A_{al} = d_{k,DPF}^2 - (d_{k,DPF} - 2\delta_{al})^2 = 4\delta_{al}(d_{k,DPF} - \delta_{al}) \\ A_{pl} = (d_{k,DPF} - 2\delta_{al})^2 - [d_{k,DPF} - 2(\delta_{al} + \delta_{pl})]^2 = 4\delta_{pl}(d_{k,DPF} - 2\delta_{al} - \delta_{pl}) \end{cases} \quad (7)$$

$$\begin{cases} m_{al} = A_{al}L_{DPF}\rho_{al} \\ m_{pl} = A_{pl}L_{DPF}\rho_{pl} \end{cases} \quad (8)$$

Furthermore,

$$\delta_{al} = \frac{d_{k,DPF}}{2} - \frac{1}{2}\sqrt{d_{k,DPF}^2 - \frac{m_{al}}{L_{DPF}\rho_{al}}} \quad (9)$$

$$\delta_{pl} = \frac{1}{2}\sqrt{d_{k,DPF}^2 - \frac{m_{al}}{L_{DPF}\rho_{al}}} - \frac{1}{2}\sqrt{d_{k,DPF}^2 - \frac{1}{L_{DPF}}\left(\frac{m_{al}}{\rho_{al}} + \frac{m_{pl}}{\rho_{pl}}\right)} \quad (10)$$

where ρ_{al} and ρ_{pl} are the particle packing density in ash layer and particulate layer, respectively. σ_{DPF} is the cell density.

$$N_{ch,DPF} = \frac{\pi D_{DPF}^2 \sigma_{DPF}}{8 \cdot 0.0254^2} = 193.75 \pi D_{DPF}^2 \sigma_{DPF} \quad (11)$$

where N_{ch} is the total number of inlet channels. D_{DPF} is the substrate

diameter.

2.2. Mechanism of collector unit growth

Fig. 3 shows the growth diagram of the collector unit. The current wall layer porosity (ϵ_{wl}) is calculated by considering the increase of collector unit diameter from the initial value ($d_{f,0}$) to the current value ($d_{f,wl}$): [22,47]

$$\epsilon_{wl} = 1 - \left(\frac{d_{f,wl}}{d_{f,0}}\right)^3 (1 - \epsilon_{DPF,0}) \quad (12)$$

The $d_{f,wl}$ is expressed as [3]

$$d_{f,wl} = 2 \left[\frac{3m_{f,wl}}{4\pi\chi\rho_{wl}} + \left(\frac{d_{f,0}}{2}\right)^3 \right]^{1/3} \quad (13)$$

where $m_{f,wl}$ is the PM mass in cell unit, ρ_{wl} is the PM packing density in wall layer, and χ is the shape factor. The lower the χ is, the more irregular the particles are deposited around the collector unit. When $\chi = 1$, it indicates that the deposited particles grow uniformly on the surface of the collector unit [48].

The saturation PM mass of single cell unit is obtained as [21]

$$m_{sat,cell} = \frac{\pi}{6} \left[(\psi d_{cell})^3 - d_{f,0}^3 \right] \rho_s \quad (14)$$

The total number of saturated units is given by [21]

$$N_{cell,sat} = \frac{m_{sat,wl}}{m_{sat,cell}} \quad (15)$$

2.3. Analysis of pressure drop composition

As shown in Fig. 4, the overall DPF pressure drop is mainly divided into the following parts. (i) Inertial loss, composed of the contraction pressure (ΔP_{con}) from the expansion tube into the inlet channel and the expansion pressure (ΔP_{exp}) from the outlet channel into the contraction tube; (ii) Friction loss, composed of pressure drop of inlet channel (ΔP_{in}) and outlet channel (ΔP_{out}); (iii) Cake and wall layer, composed of

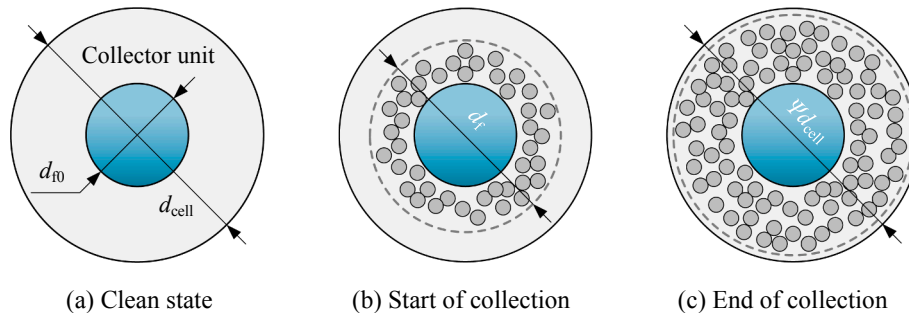


Fig. 3. Growth diagram of the collector unit.

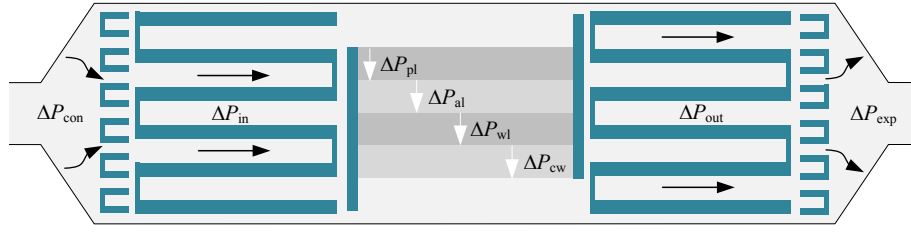


Fig. 4. DPF pressure composition diagram.

pressure drop of particulate layer (ΔP_{pl}), ash layer (ΔP_{al}), wall layer (ΔP_{wl}), and clean wall layer (ΔP_{cw}).

The relationship between the pressure drop of each part is expressed as

$$\Delta P_{tot} = \Delta P_{con} + \Delta P_{exp} + \Delta P_{in} + \Delta P_{out} + \Delta P_{load} \quad (16)$$

$$\Delta P_{load} = \Delta P_{pl} + \Delta P_{al} + \Delta P_{wl} + \Delta P_{cw} \quad (17)$$

where ΔP_{tot} is the overall pressure drop, and ΔP_{load} is the pressure drop formed by the wall and cake.

$$\Delta P_{con} = \frac{1}{2} \xi_{con} \rho_g u_{in}^2 \quad (18)$$

$$\Delta P_{exp} = \frac{1}{2} (1 - \lambda_r)^2 \rho_g u_{out}^2 = \frac{1}{2} \xi_{exp} \rho_g u_{out}^2 \quad (19)$$

$$\xi_{tot} = \xi_{con} + \xi_{exp} = \frac{1}{C^2} (1 - \lambda_r)^2 \quad (20)$$

where ξ_{con} is the dimensionless contraction coefficient, ξ_{exp} is the dimensionless expansion coefficient, and their value ranging from 0.3 to 1.24 mainly depend on porosity of substrate and Reynolds number. When the cell density is 100 or 200, λ_r generally takes the value 0.35. C is a constant depending on Reynolds number, cell density and porosity, which is set to 0.82.

The exhaust flow in the channel is considered to be incompressible laminar flow. ΔP_{in} and ΔP_{out} are expressed as

$$\Delta P_{in} = \frac{1}{3} F_{w,in} \mu L_{DPF} \frac{u_{in}}{[d_{k,DPF} - 2(\delta_{pl} + \delta_{al})]^2} \quad (21)$$

$$\Delta P_{out} = \frac{1}{3} F_{w,out} \mu L_{DPF} \frac{u_{out}}{d_{k,DPF}^2} \quad (22)$$

where F_w is viscosity loss coefficient or friction loss coefficient, and the value in this study is set to 28.454 [52].

2.4. Establishment of equivalent permeability model for each stage

The pressure drop of DPF can be calculated by Darcy's law and Forchheimer term [53]. For high flow velocity, considering the inertial losses, the Forchheimer term needs to be added. The magnitude of the Forchheimer term for the pressure drop of cake and wall layer is small and has little effect on the overall pressure drop, so this item is discarded in this study.

2.4.1. Deep bed collection stage

According to Darcy's law, ΔP_{wl} and ΔP_{cw} are expressed as

$$\Delta P_{wl} = \frac{\mu_{wl} u_{wl} \delta_{wl}}{k_{wl}} \quad (23)$$

$$\Delta P_{cw} = \frac{\mu_{cw} u_{cw} (\delta_w - \delta_{wl})}{k_{cw}} \quad (24)$$

where δ_{wl} and μ_{cw} are the exhaust dynamic viscosity flowing through

wall layer and clean layer, respectively. u_{wl} and u_{cw} are the exhaust penetration speed in wall layer and clean wall, respectively. k_{wl} and k_{cw} are the permeability of wall layer and clean wall, respectively.

The volume flow through porous media with one face in a single channel is $Q_{v,ch}$.

$$Q_{v,ch}(z) = \frac{3.584 \times 10^{-7} Q_m}{\pi \sigma_{DPF} \rho_g(z) D_{DPF}^2} \quad (25)$$

$$\rho_g(z) = \frac{P(z)}{R_g T_g(z)} \quad (26)$$

where Q_m is the inlet exhaust mass flow, D_{DPF} is the substrate diameter, ρ_g is the exhaust density, P is the local absolute pressure, R_g is the special gas constant of exhaust, T_g is the exhaust temperature, and z is the distance from the porous medium inlet plane.

In actual diesel engine operation conditions, the time required for exhaust to pass through porous medium is generally on the order of 10^{-5} s. If the operating conditions are not too transient, the exhaust mass flow through the porous medium can be considered constant at a certain moment. Therefore, $T_g(z)$ and $P(z)$ take the average value of inlet and outlet of porous medium.

$$\begin{cases} P_{con} = [P(0) + P(\delta_c + \delta_{w,DPF})]/2 \\ T_{g,con} = [T_g(0) + T_g(\delta_c + \delta_{w,DPF})]/2 \end{cases} \quad (27)$$

Therefore,

$$u_{wl} = u_{cw} = \frac{Q_{v,ch}}{d_{k,DPF} L_{DPF}} \quad (28)$$

In low-viscosity fluids, the drag force acting on collector unit can be given by Stokes' law [25]. C_s is the Stokes-Cunningham factor, determining the slip flow effect and the drag force correction value [25].

$$F_{wl} = \frac{3\pi\mu_{wl}u_{wl}d_{f,wl}}{\epsilon_{wl}C_{s,wl}} \quad (29)$$

$$F_{cw} = \frac{3\pi\mu_{cw}u_{cw}d_{f,cw}}{\epsilon_{DPF,0}C_{s,cw}} \quad (30)$$

It should be noted that the filtration velocity of the exhaust in the porous medium is the permeability velocity [25,53]. The pore velocity is calculated by formula u_w/ϵ_w . It should be noted that this value has a different meaning from the penetration velocity in Darcy's law. C_s depends on the Knudsen number (K_n) [25,53], and the latter is a function of gas mean free path (λ) and d_{pore} .

$$C_s = 1 + K_n \left[1.257 + 0.4 \exp\left(-\frac{1.1}{K_n}\right) \right] \quad (31)$$

$$K_{n,wl} = \frac{2\lambda}{d_{pore,wl}} \quad (32)$$

$$K_{n,cw} = \frac{2\lambda}{d_{pore,cw}} \quad (33)$$

$$\lambda = \mu \sqrt{\frac{\pi}{2P\rho_g}} \quad (34)$$

where λ is in interval $[10^{-8}, 10^{-7}]$ m, and the value of λ in this study is 65 nm.

As shown in Fig. 5, the number of collector units in wall layer and clean layer is $N_{\text{cell,wl}}$ and $N_{\text{cell,cw}}$ respectively, and the total number of collector units is $N_{\text{cell,w}}$,

$$N_{\text{cell,wl}} = \frac{6d_{k,\text{DPF}}L_{\text{DPF}}\delta_{\text{wl}}(1 - \varepsilon_{\text{DPF},0})}{\pi d_{f,0}^3} \quad (35)$$

$$N_{\text{cell,cw}} = \frac{6d_{k,\text{DPF}}L_{\text{DPF}}(\delta_{\text{w,DPF}} - \delta_{\text{wl}})(1 - \varepsilon_{\text{DPF},0})}{\pi d_{f,0}^3} \quad (36)$$

$$N_{\text{cell,w}} = N_{\text{cell,wl}} + N_{\text{cell,cw}} \quad (37)$$

The resistance F_c acts on the wall containing $N_{\text{cell,w}}$ collector units, and the pressure drop acts on the exhaust through the counter resistance. Therefore,

$$\Delta P_{\text{wl}} = \frac{N_{\text{cell,wl}}F_{\text{wl}}}{d_{k,\text{DPF}}L_{\text{DPF}}} \quad (38)$$

$$\Delta P_{\text{cw}} = \frac{N_{\text{cell,cw}}F_{\text{cw}}}{d_{k,\text{DPF}}L_{\text{DPF}}} \quad (39)$$

Therefore,

$$k_{\text{wl}} = \frac{C_{S,\text{wl}}\varepsilon_{\text{wl}}d_{f,0}^2}{18d_{f,\text{wl}}(1 - \varepsilon_{\text{DPF},0})} \quad (40)$$

$$k_{\text{cw}} = \frac{C_{S,\text{cw}}\varepsilon_{\text{DPF},0}d_{f,0}^2}{18(1 - \varepsilon_{\text{DPF},0})} \quad (41)$$

$$\Delta P_{\text{w}} = \frac{\mu_{\text{w}}u_{\text{w}}\delta_{\text{DPF}}}{k_{\text{w,ef}}} = \frac{\mu_{\text{wl}}u_{\text{wl}}\delta_{\text{wl}}}{k_{\text{wl}}} + \frac{\mu_{\text{cw}}u_{\text{cw}}(\delta_{\text{DPF}} - \delta_{\text{wl}})}{k_{\text{cw}}} \quad (42)$$

Wall equivalent permeability is $k_{\text{w,ef}}$, which is expressed as

$$k_{\text{w,ef}} = \frac{k_{\text{wl}}k_{\text{cw}}}{f_{\text{wl}}k_{\text{cw}} + (1 - f_{\text{wl}})k_{\text{wl}}} \quad (43)$$

$$f_{\text{wl}} = \frac{\delta_{\text{wl}}}{\delta_{\text{DPF}}} \quad (44)$$

where f_{wl} is the ratio of wall layer thickness to total wall thickness.

2.4.2. Cake collection stage

According to Darcy's law, ΔP_{pl} and ΔP_{al} are expressed as

$$\Delta P_{\text{pl}} = \frac{\mu_{\text{pl}}}{k_{\text{pl}}} \int u_{\text{pl}}(z) dz \quad (45)$$

$$\Delta P_{\text{al}} = \frac{\mu_{\text{al}}}{k_{\text{al}}} \int u_{\text{al}}(z) dz \quad (46)$$

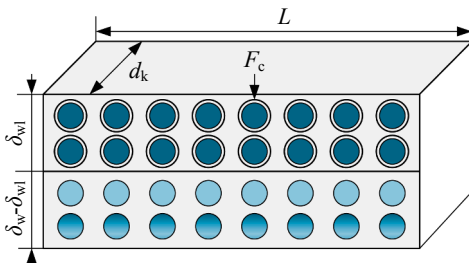


Fig. 5. Force acting on the collector unit.

where μ_{pl} and μ_{al} are the exhaust dynamic viscosity flowing through particulate layer and ash layer, respectively. u_{pl} and u_{al} are the penetration speed of the exhaust in particulate layer and ash layer, respectively. k_{pl} and k_{al} are the permeability of particulate layer and ash layer, respectively.

$u(z)$ is the penetration velocity exhaust in the filter cake layer, which is expressed as

$$u(z) = \frac{Q_{v,\text{ch}}}{[d_{k,\text{DPF}} - 2(\delta_{\text{pl}} + \delta_{\text{al}}) + 2z]L_{\text{DPF}}} \quad (47)$$

$$\begin{cases} u_{\text{pl}}(z) = u(z), & z \in [0, \delta_{\text{pl}}] \\ u_{\text{al}}(z) = u(z), & z \in [\delta_{\text{pl}}, \delta_{\text{pl}} + \delta_{\text{al}}] \end{cases} \quad (48)$$

Therefore,

$$\Delta P_{\text{pl}} = \frac{\mu_{\text{pl}}Q_{v,\text{ch}}}{2k_{\text{pl}}L_{\text{DPF}}} \ln \left[\frac{d_{k,\text{DPF}} - 2\delta_{\text{al}}}{d_{k,\text{DPF}} - 2(\delta_{\text{pl}} + \delta_{\text{al}})} \right] \quad (49)$$

$$\Delta P_{\text{al}} = \frac{\mu_{\text{al}}Q_{v,\text{ch}}}{2k_{\text{al}}L_{\text{DPF}}} \ln \left(\frac{d_{k,\text{DPF}}}{d_{k,\text{DPF}} - 2\delta_{\text{al}}} \right) \quad (50)$$

The forces acting on the collector units of particulate layer and ash layer are F_{pl} and F_{al} respectively, which are expressed as

$$F_{\text{pl}} = \frac{3\pi\mu_{\text{pl}}u_{\text{pl}}d_{f,\text{pl}}}{\varepsilon_{\text{pl}}C_{S,\text{pl}}} \quad (51)$$

$$F_{\text{al}} = \frac{3\pi\mu_{\text{al}}u_{\text{al}}d_{f,\text{al}}}{\varepsilon_{\text{al}}C_{S,\text{al}}} \quad (52)$$

$$K_{n,\text{pl}} = \frac{2\lambda}{d_{\text{pore,pl}}} \quad (53)$$

$$K_{n,\text{al}} = \frac{2\lambda}{d_{\text{pore,al}}} \quad (54)$$

The number of collector units in particulate layer and ash layer is $N_{\text{cell,pl}}$ and $N_{\text{cell,al}}$ respectively, and the total number of collector units is $N_{\text{cell,c}}$.

$$N_{\text{cell,pl}} = \frac{6\delta_{\text{pl}}(d_{k,\text{DPF}} - 2\delta_{\text{al}} - \delta_{\text{pl}})L_{\text{DPF}}(1 - \varepsilon_{\text{pl}})}{\pi d_{f,\text{pl}}^3} \quad (55)$$

$$N_{\text{cell,al}} = \frac{6\delta_{\text{al}}(d_{k,\text{DPF}} - \delta_{\text{al}})L_{\text{DPF}}(1 - \varepsilon_{\text{al}})}{\pi d_{f,\text{al}}^3} \quad (56)$$

$$N_{\text{cell,c}} = N_{\text{cell,pl}} + N_{\text{cell,al}} \quad (57)$$

The resistance F_{pl} and F_{al} acts on the cake containing $N_{\text{cell,c}}$ collector units, and the pressure drop acts on the exhaust through the counter resistance.

$$F_{\text{pl}} = \frac{3\pi\mu_{\text{pl}}u_{\text{pl}}d_{f,\text{pl}}}{\varepsilon_{\text{pl}}C_{S,\text{pl}}} \quad (58)$$

$$F_{\text{al}} = \frac{3\pi\mu_{\text{al}}u_{\text{al}}d_{f,\text{al}}}{\varepsilon_{\text{al}}C_{S,\text{al}}} \quad (59)$$

Therefore,

$$k_{\text{pl}} = \frac{C_{S,\text{pl}}\varepsilon_{\text{pl}}d_{f,\text{pl}}^2}{36(1 - \varepsilon_{\text{pl}})} \frac{(d_{k,\text{DPF}} - 2\delta_{\text{al}} - \delta_{\text{pl}})}{\delta_{\text{pl}}} \ln \left[\frac{d_{k,\text{DPF}} - 2\delta_{\text{al}}}{d_{k,\text{DPF}} - 2(\delta_{\text{pl}} + \delta_{\text{al}})} \right] \quad (60)$$

$$k_{\text{al}} = \frac{C_{S,\text{al}}\varepsilon_{\text{al}}d_{f,\text{al}}^2}{36(1 - \varepsilon_{\text{al}})} \frac{(d_{k,\text{DPF}} - \delta_{\text{al}})}{\delta_{\text{al}}} \ln \left(\frac{d_{k,\text{DPF}}}{d_{k,\text{DPF}} - 2\delta_{\text{al}}} \right) \quad (61)$$

The following assumptions are given by,

$$y_{pl} = \frac{(d_{k,DPF} - 2\delta_{al} - \delta_{pl})}{\delta_{pl}} \ln \left[\frac{d_{k,DPF} - 2\delta_{al}}{d_{k,DPF} - 2(\delta_{pl} + \delta_{al})} \right] \quad (62)$$

$$y_{al} = \frac{(d_{k,DPF} - \delta_{al})}{\delta_{al}} \ln \left(\frac{d_{k,DPF}}{d_{k,DPF} - 2\delta_{al}} \right) \quad (63)$$

Therefore,

$$k_{pl} = \frac{C_{S,pl} \varepsilon_{pl} d_{f,pl}^2}{18(1 - \varepsilon_{pl})} \quad (64)$$

$$k_{al} = \frac{C_{S,al} \varepsilon_{al} d_{f,al}^2}{18(1 - \varepsilon_{al})} \quad (65)$$

2.5. Calculation of soot loading

The function $g(\delta_c)$ is constructed as follows,

$$g(\delta_c) = \frac{b_1}{(d_{k,DPF} - 2\delta_c)^4} + \frac{b_2}{(d_{k,DPF} - 2\delta_c)^4} + b_3 \ln \left(\frac{d_{k,DPF} - 2f_{al}\delta_c}{d_{k,DPF} - 2\delta_c} \right) + b_4 \ln \left(\frac{d_{k,DPF}}{d_{k,DPF} - 2f_{al}\delta_c} \right) - b_0 \quad (66)$$

Where $b_j (0 \leq j \leq 4)$ is expressed as,

$$b_0 = \Delta P_{tot} - \frac{\mu_{wl} u_{wl} \delta_{wl}}{k_{wl}} - \frac{\mu_{cw} u_{cw} (\delta_{DPF} - \delta_{wl})}{k_{cw}} - \frac{8\varepsilon_{exp} \rho_g Q_{v,ch}^2}{d_{k,DPF}^4} - \frac{4F_{w,out} \mu L_{DPF} Q_{v,ch}}{3d_{k,DPF}^4} \quad (67)$$

$$b_1 = 8\varepsilon_{con} \rho_g Q_{v,ch}^2 \quad (68)$$

$$b_2 = \frac{4}{3} F_{w,in} \mu L_{DPF} Q_{v,ch} \quad (68)$$

$$b_3 = \frac{\mu_{pl} Q_{v,ch}}{2k_{pl} L_{DPF}} \quad (70)$$

$$b_4 = \frac{\mu_{al} Q_{v,ch}}{2k_{al} L_{DPF}} \quad (71)$$

Therefore, the zero point of $g(\delta_c)$ is the value of δ_c . $g(\delta_c)$ is a transcendental equation, and it is difficult to find analytical solution. In this study, numerical solution is found through Taylor's formula in this study. The function $g(\delta_c) = 0$ can be transformed into,

$$\frac{b_1 + b_2}{(d_{k,DPF} - 2\delta_c)^4} + (b_3 - b_4) \ln(d_{k,DPF} - 2f_{al}\delta_c) - b_3 \ln(d_{k,DPF} - 2\delta_c) - b_0 + b_4 \ln d_{k,DPF} = 0 \quad (72)$$

The overall soot loading is M_I , the deep bed soot loading threshold is M_d , and the cake soot loading is M_c , which are expressed as

$$M_I = M_d + M_c \quad (73)$$

$$M_c = M_{al} + M_{pl} \quad (74)$$

$$M_{al} = \frac{4 \times 10^3 \rho_{al} f_{al} d_c (d_{k,DPF} - f_{al}\delta_c) L_{DPF} N_{ch}}{V_{DPF}} \quad (75)$$

$$M_{pl} = \frac{4 \times 10^3 \rho_{pl} (1 - f_{al}) \delta_c [d_{k,DPF} - (1 + f_{al}) \delta_c] L_{DPF} N_{ch}}{V_{DPF}} \quad (76)$$

3. Experimental layout and model verification

3.1. Experimental layout

The model verification test was performed on a heavy-duty diesel

engine. Detailed engine specifications are shown in Table 1.

The layout of bench test system is shown in Fig. 6. The engine is connected with electric dynamometer and AVL-PUMA automatic measurement system, which can perform at certain torque and speed and automatically record data. HAQ-A30 is used to measure the DPF mass, the maximum measuring mass of this instrument is 30 kg, and the measuring error is ± 0.2 g.

The key technical parameters of DPF are shown in Table 2.

3.2. Soot loading procedure

The soot loading procedures and pressure drop measurement are as follows,

- The initial mass of clean DPF was measured using HAQ-A30 and recorded as M_0 , and then start DPF loading.
- The loading cycle is a self-defined transient cycle with a duration of 3455 s. The characteristic parameters of the self-defined transient loading cycle are shown in Fig. 7 and Fig. 8.
- The test results show that compared with the WHTC cycle, the self-defined cycle has fewer high temperature conditions. Under self-defined cycle, the exhaust temperature is basically maintained below 250 °C, which is conducive to the rapid soot loading.
- The DPF is weighed once every 10 cycles, and the weight is recorded as M_1 . The DPF was weighed 5 times in total, and the maximum and minimum weighing values were removed to ensure accurate results. The average value of the remaining three times was taken.
- After weighing, DPF was added to measure the pressure drop characteristics under steady-state conditions. The torque was 400 N·m, and the speed was set to 600 r/min, 1100 r/min, 1500 r/min, 1800 r/min, and 2200 r/min respectively. The pressure drop and other data were measured after each operating condition was stabilized for 2 to 3 min.
- Repeat the steps (ii) and (iii), and measure pressure drop under four different soot loading.

3.3. Results of experiment and verification

The current soot loading is calculated by

$$M_{I,exp} = \frac{M_1 - M_0}{V_{DPF}} \quad (77)$$

where V_{DPF} is the DPF volume, M_0 is 12248 g, M_1 is the current DPF mass, and $M_{I,exp}$ is the soot loading in the test. The loading process and weighing records are shown in Fig. 9.

The measurement and prediction results are shown in Fig. 10. The maximum prediction error is less than 5%, and the average error is 2.72%. The prediction accuracy of the model is within a reasonable range.

Table 1
Engine specifications.

Parameter	Value
Displacement	8.82 L
Rated power	184 kW (2200 r/min)
Compression ratio	18:1
Cylinder number	6
Maximum torque	1000 N·m (1400 r/min)
Air-intake system	Turbocharger with intercooler
Fuel system	Common rail

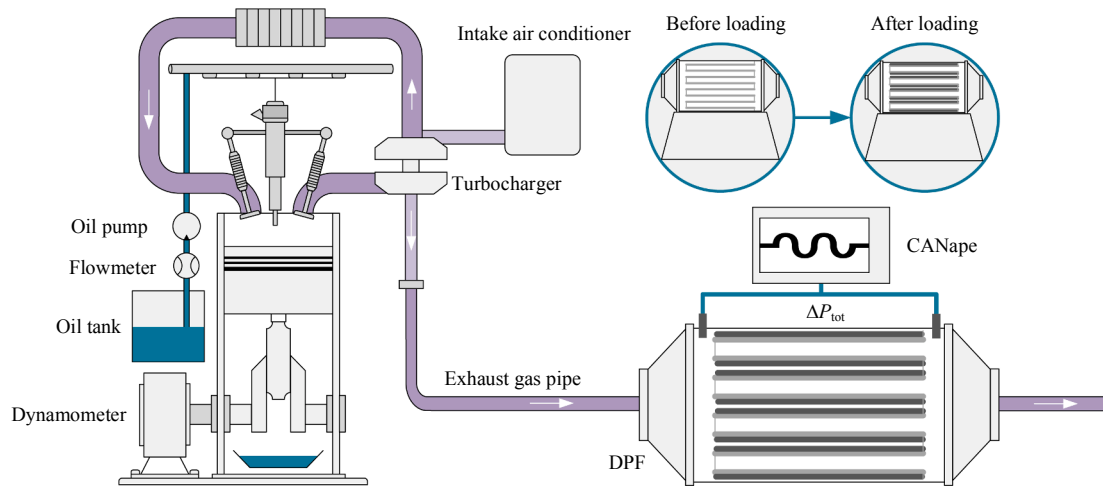


Fig. 6. Schematic diagram of bench test.

Table 2

Technical parameters of DPF.

Parameter	Value
Volume	14.22 L
Length	254 mm
Cell density	200 cpsi
Main material	Cordierite
Wall thickness	0.30 mm
Channel type	Wall flow

4. Results and discussion

4.1. Effects of DPF diameter and length on soot loading characteristics

Set mass flow and exhaust temperature to 950 kg/h and 295 °C, respectively, set cell density and wall thickness to 200 cpsi and 0.3 mm, respectively, select 307 mm, 267 mm, and 227 mm for diameter, and select 294 mm, 254 mm, and 214 mm for length. Keep the diameter unchanged, reduce the length in turn, and then reduce the diameter, and these cases are named 1-1, 1-2, 1-3, 2-1, 2-2, 2-3, 3-1, 3-2, and 3-3, respectively. Fig. 11 shows the effects of DPF diameter and length on soot loading.

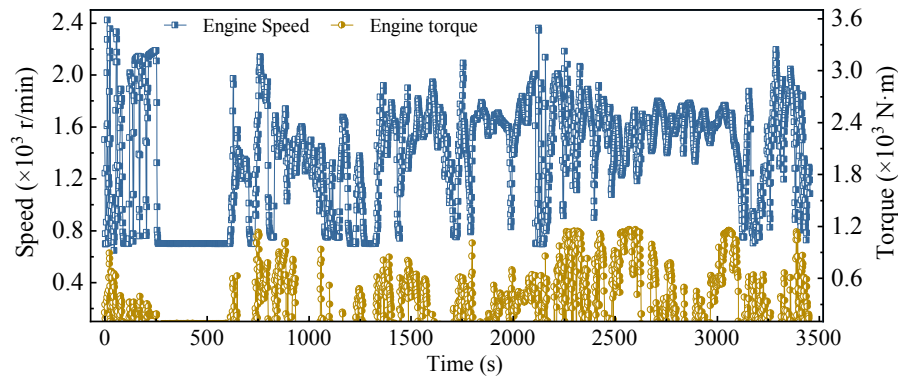


Fig. 7. Operating conditions for soot loading cycle.

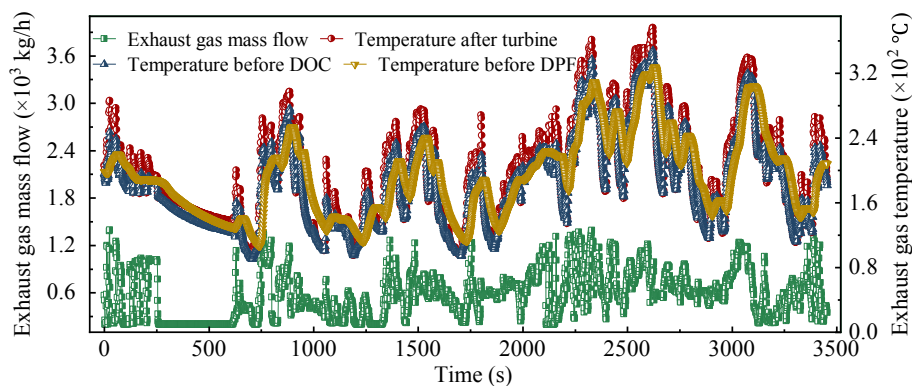


Fig. 8. Exhaust mass flow and temperature under loading cycle.

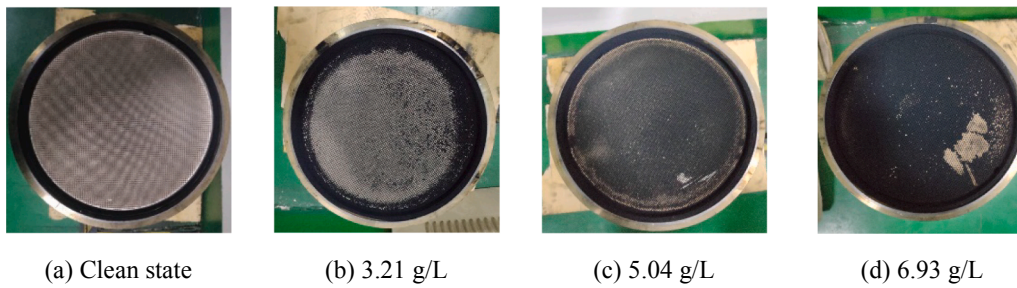


Fig. 9. Soot loading process.

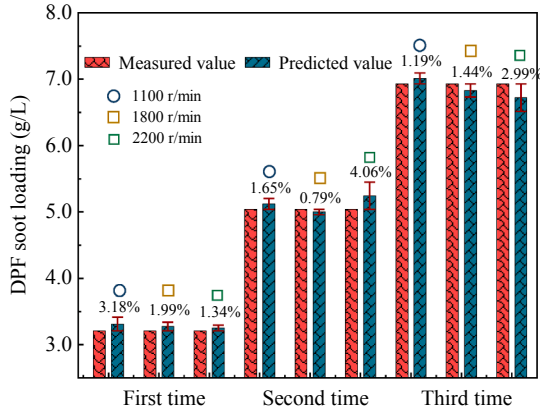


Fig. 10. Model prediction results.

The effect of DPF diameter on the soot loading is greater than the effect of length under a certain pressure drop. The larger the diameter and length, the greater the soot loading. Under the condition of low pressure drop, when the diameter is 227 mm, the soot loading is close to 0, and when the diameter is 307 mm, the soot loading is above 2 g/L. Fig. 12 shows the influence of diameter and length on the relationship between soot loading and pressure drop.

In the case of two pressure drops, the cake layer pressure drop is the most important component. Under the higher pressure drop, the cake layer accounts for a higher proportion. As the length increases and the diameter decreases, the cake layer pressure drop slightly decreases. Under the same structural parameters, an increase in soot loading means an increase in the mass of deposited particles, an increase in the cake layer thickness, and an increase in the cake layer pressure drop proportion. As the length increases, the friction loss increases. As the length increases, the effective penetration area decreases, the penetration

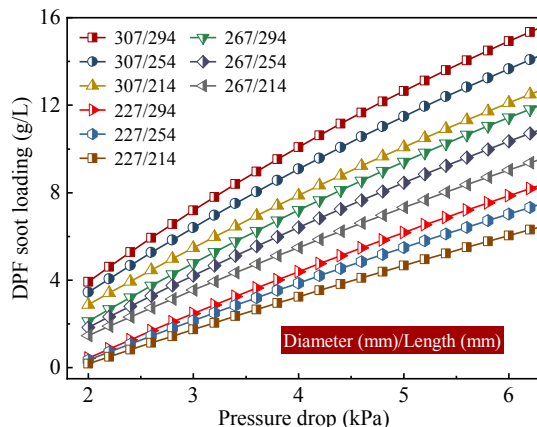


Fig. 11. The effects of DPF diameter and length on soot loading.

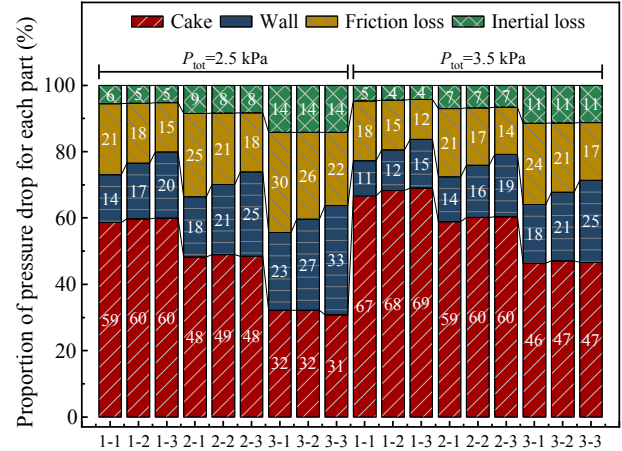


Fig. 12. The influence of diameter and length on the relationship between soot loading and pressure drop.

velocity decreases, and the wall pressure drop decreases. These two effects cancel each other out, resulting in little change in the proportion of cake layer pressure drop.

However, as the diameter decreases, the single-channel exhaust volume flow increases, the wall gas flow velocity increases, and the friction loss and inertial loss will increase, the penetration velocity will increase, and the wall pressure drop will increase. This effect is more pronounced when the overall pressure drop is at a lower level, because if the overall pressure is reduced, the change of DPF inherent structural parameters other than particle deposition has a greater impact on the overall pressure drop.

4.2. Effects of cell density and wall thickness on soot loading characteristics

Set mass flow and exhaust temperature to 950 kg/h and 295 °C, respectively, set diameter and lengths to 267 mm and 254 mm, respectively, select 300 cpsi, 200 cpsi, and 100 cpsi for cell density, and select 0.4 mm, 0.3 mm, and 0.2 mm for wall thickness. Keep the cell density unchanged, reduce the wall thickness in turn, and then reduce the cell density, and these cases are named 1-1, 1-2, 1-3, 2-1, 2-2, 2-3, 3-1, 3-2, and 3-3, respectively. Fig. 13 shows the effects of cell density and wall thickness on soot loading.

Keep the cell density constant, as the wall thickness decreases, the soot loading under the same pressure drop increases. However, under the premise of the same pressure drop, the influence of wall thickness on soot loading presents an inconsistent law. When the wall thickness is 0.3 mm and 0.2 mm, as the cell density decreases, the soot loading increases under the premise of the same pressure drop. When the pressure drop is greater than 3.25 kPa and the wall thickness is 0.4 mm, the corresponding soot loading at 200 cpsi is higher than that at 100 cpsi and 300 cpsi. Fig. 14 shows the influence of cell density and wall thickness on the

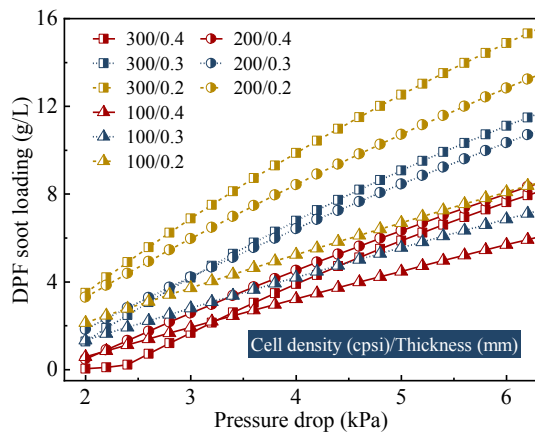


Fig. 13. The effects of cell density and wall thickness on soot loading.

relationship between soot loading and pressure drop.

With the decrease of wall thickness, the proportion of wall pressure drop, inertial loss and friction loss all decrease, so the cake pressure drop increases greatly. This trend is more pronounced in the case of high cell density and low pressure drop values. As the cell density decreases, the wall pressure drop increases, and the inertial loss and friction loss decrease. The amplitude of the friction loss is the largest. This shows that the change of exhaust flow velocity in the channel has a greater impact on the friction loss.

4.3. Effects of mass flow and temperature of exhaust on soot loading characteristics

Set cell density and wall thickness to 200 cpsi and 0.3 mm, respectively, set diameter and lengths to 267 mm and 254 mm, respectively, select 1450 kg/h, 950 kg/h, and 450 kg/h for mass flow, and select 395 °C, 295 °C, and 195 °C for exhaust temperature. Keep the mass flow unchanged, reduce the exhaust temperature in turn, and then reduce the mass flow, and these cases are named 1-1, 1-2, 1-3, 2-1, 2-2, 2-3, 3-1, 3-2, and 3-3, respectively. Fig. 15 shows the effects of mass flow and temperature on soot loading.

In general, the soot loading is higher at low exhaust flow. This is because the low exhaust flow means that the exhaust volume flow of single channel is low, and the channel wall flow velocity and permeation velocity decrease. If the total pressure drop is kept constant, the particle deposition will increase. When the exhaust mass flow is kept constant, the exhaust temperature decreases, the volume flow decreases, the

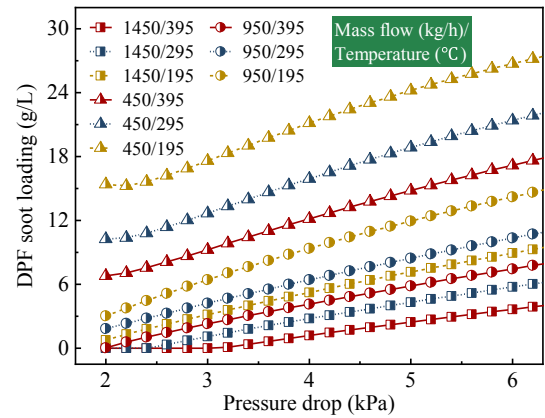


Fig. 15. The effects of mass flow and temperature on soot loading.

channel wall flow velocity and permeation velocity decrease, and the proportion of cake pressure drop increases. Therefore, the soot loading also increases. Fig. 16 shows the influence of mass flow and exhaust gas temperature on the relationship between soot loading and pressure drop.

Under the conditions of low exhaust mass flow and low exhaust temperature, the proportion of the pressure drop for each part is less affected by the engine operating parameters and the overall pressure drop. Exhaust mass flow and temperature mainly change the flow state of exhaust in the channel, cake layer and wall by changing the volume flow, thereby changing the pressure drop value for each part. During active regeneration, the exhaust temperature rises rapidly, so that the volume flow changes rapidly, and the pressure drop proportion for each part also changes rapidly. Therefore, the prediction of soot loading under regeneration conditions has more complexity.

5. Conclusions

The following main conclusions can be drawn in this study:

- Novel soot loading prediction model of diesel particulate filter based on collection mechanism and equivalent permeability is proposed. Firstly, based on the DPF packed bed collection mechanism, collector unit growth model affected by the deposited particles is established, and then equivalent permeation filtration model considering the deep bed and cake collection stage is established.

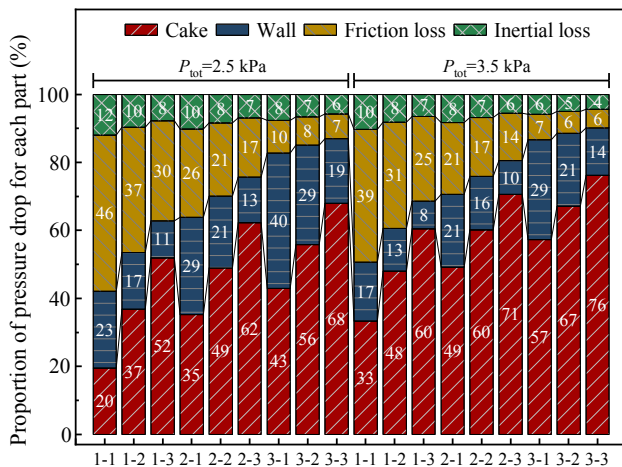


Fig. 14. The influence of cell density and wall thickness on the relationship between soot loading and pressure drop.

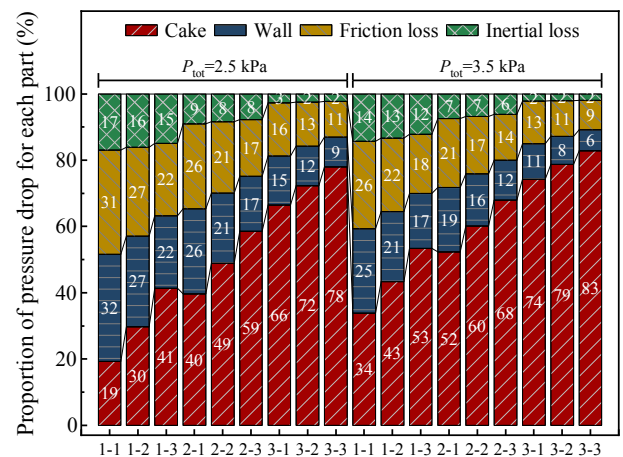


Fig. 16. The influence of mass flow and exhaust gas temperature on the relationship between soot loading and pressure drop.

- (ii) The DPF overall pressure drop model is divided into inertial loss, friction loss, and multilayer cake and wall layer pressure drop. Finally, the overall soot loading equation is established and the numerical solution is solved by Taylor's formula. The model is verified by bench test, the maximum prediction error is less than 5%, and the average error is 2.72%.
- (iii) The effect of DPF diameter on the soot loading is greater than the effect of length under a certain pressure drop. Under the higher pressure drop, the cake layer accounts for a higher proportion. As the length increases, the effective penetration area decreases, the penetration velocity decreases, and the wall pressure drop decreases. These two effects cancel each other out, resulting in little change in the proportion of cake layer pressure drop.
- (iv) With the decrease of wall thickness, the proportion of wall pressure drop, inertial loss and friction loss all decrease, so the cake pressure drop increases greatly. This trend is more pronounced in the case of high cell density and low pressure drop values. When the exhaust gas mass flow is kept constant, the exhaust gas temperature decreases, and the proportion of cake pressure drop increases. In the case of active regeneration, the exhaust gas temperature rises rapidly, so that the volume flow changes rapidly, and the pressure drop proportion for each part also changes rapidly.

CRedit authorship contribution statement

De-yuan Wang: Conceptualization, Methodology, Validation, Resources, Supervision, Writing - review & editing, Funding acquisition. **Pi-qiang Tan:** Conceptualization, Methodology, Formal analysis, Writing - original draft, Writing - review & editing. **Lei Zhu:** Methodology, Validation, Supervision, Project administration. **Yin-huan Wang:** Supervision, Project administration, Funding acquisition. **Zhi-yuan Hu:** Conceptualization, Methodology, Investigation. **Di-ming Lou:** Methodology, Validation, Formal analysis.

Declaration of Competing Interest

The authors declare that they have no known competing financial interests or personal relationships that could have appeared to influence the work reported in this paper.

Acknowledgment

This work was supported by the National Key R&D Program of China (No. 2017YFC0211202).

References

- [1] Che Mat S, Idroas MY, Hamid MF, et al. Performance and emissions of straight vegetable oils and its blends as a fuel in diesel engine: A review. *Renew Sustain Energy Rev* 2018;82:808–23.
- [2] Liu J, Sun P, Huang H, et al. Experimental investigation on performance, combustion and emission characteristics of a common-rail diesel engine fueled with polyoxymethylene dimethyl ethers-diesel blends. *Appl Energy* 2017;202: 527–36.
- [3] Tan P, Wang D, Yao C, et al. Extended filtration model for diesel particulate filter based on diesel particulate matter morphology characteristics. *Fuel* 2020;277: 118150.
- [4] Fiebig M, Wiartalla A, Holderbaum B, et al. Particulate emissions from diesel engines: correlation between engine technology and emissions. *J Occupat Med Toxicol* 2014;9(1):1–18.
- [5] Jain A, Singh AP, Agarwal AK. Effect of split fuel injection and EGR on NOx and PM emission reduction in a low temperature combustion (LTC) mode diesel engine. *Energy* 2017;122:249–64.
- [6] Saxena MR, Maurya RK. Effect of premixing ratio, injection timing and compression ratio on nano particle emissions from dual fuel non-road compression ignition engine fueled with gasoline/methanol (port injection) and diesel (direct injection). *Fuel* 2017;203:894–914.
- [7] Barrios CC, Domínguez-Sáez A, Hormigo D. Influence of hydrogen addition on combustion characteristics and particle number and size distribution emissions of a TDI diesel engine. *Fuel* 2017;199:162–8.
- [8] Finesso R, Misul D, Spessa E. Development and validation of a semi-empirical model for the estimation of particulate matter in diesel engines. *Energy Convers Manage* 2014;84:374–89.
- [9] Tan P, Li Y, Shen H. Exhaust particle properties from a light duty diesel engine using different ash content lubricating oil. *J Energy Inst* 2018;91(1):55–64.
- [10] Wang Y, Liang X, Tang G, et al. Impact of lubricating oil combustion on nanostructure, composition and graphitization of diesel particles. *Fuel* 2017;190: 237–44.
- [11] Karin P, Boonsakda J, Siricholathum K, et al. Morphology and oxidation kinetics of CI engine's biodiesel particulate matters on cordierite Diesel Particulate Filters using TGA. *Int J Automot Technol* 2017;18(1):31–40.
- [12] Tan P, Li Y, Shen H. Effect of lubricant sulfur on the morphology and elemental composition of diesel exhaust particles. *J Environ Sci* 2017;55:354–62.
- [13] Man XJ, Cheung CS, Ning Z. Effect of diesel engine operating conditions on the particulate size, nanostructure and oxidation properties when using wasting cooking oil biodiesel. *Energy Procedia* 2015;66:37–40.
- [14] Liu W, Song C. Effect of post injection strategy on regulated exhaust emissions and particulate matter in a HSDI diesel engine. *Fuel* 2016;185:1–9.
- [15] Fayad MA, Tsolakis A, Fernández-Rodríguez D, et al. Manipulating modern diesel engine particulate emission characteristics through butanol fuel blending and fuel injection strategies for efficient diesel oxidation catalysts. *Appl Energy* 2017;190: 490–500.
- [16] Guan B, Zhan R, Lin H, et al. Review of the state-of-the-art of exhaust particulate filter technology in internal combustion engines. *J Environ Manage* 2015;154: 225–58.
- [17] Lizarraga L, Souentie S, Boreave A, et al. Effect of diesel oxidation catalysts on the diesel particulate filter regeneration process. *Environ Sci Technol* 2011;45(24): 10591–7.
- [18] Bermúdez V, Serrano JR, Piqueras P, et al. Pre-DPF water injection technique for pressure drop control in loaded wall-flow diesel particulate filters. *Appl Energy* 2015;140:234–45.
- [19] Bissett EJ. Mathematical model of the thermal regeneration of a wall-flow monolith diesel particulate filter. *Chem Eng Sci* 1984;39(7):1233–44.
- [20] Konstantopoulos AG, Johnson JH. Wall-flow diesel particulate filters—Their pressure drop and collection efficiency. *SAE Technical* 1989.
- [21] Payri F, Arnau FJ, Piqueras P, et al. Lumped approach for flow-through and wall-flow monolithic reactors modelling for real-time automotive applications. *SAE Technical* 2018.
- [22] Serrano JR, Climent H, Piqueras P, et al. Filtration modelling in wall-flow particulate filters of low soot penetration thickness. *Energy* 2016;112:883–98.
- [23] Konstantopoulos AG. Deposit growth dynamics: particle sticking and scattering phenomena. *Powder Technol* 2000;109(1):262–77.
- [24] Murtagh M J, Sherwood D L, Socha L S. Development of a diesel particulate filter composition and its effect on thermal durability and filtration performance. 1994.
- [25] Uenishi T, Tanaka E, Shigeno G, et al. A quasi two dimensional model of transport phenomena in diesel particulate filters—The effects of particle and wall pore diameter on the pressure drop. *SAE Technical* 2015.
- [26] Bollerhoff T, Markomanolakis I, Koltsakis G. Filtration and regeneration modeling for particulate filters with inhomogeneous wall structure. *Catal Today* 2012;188 (1):24–31.
- [27] Bensaid S, Marchisio DL, Fino D. Numerical simulation of soot filtration and combustion within diesel particulate filters. *Chem Eng Sci* 2010;65(1):357–63.
- [28] Tsujimoto D, Jin K, Fukuma T. A statistical approach to improve the accuracy of the dpf simulation model under transient conditions. *SAE Technical* 2019.
- [29] Kočí P, Isoz M, Plachá M, et al. 3D reconstruction and pore-scale modeling of coated catalytic filters for automotive exhaust gas aftertreatment. *Catal Today* 2019;320:165–74.
- [30] Zhang B, E J, Gong J, et al. Influence of structural and operating factors on performance degradation of the diesel particulate filter based on composite regeneration. *Appl Therm Eng* 2017; 121: 838–852.
- [31] Zhang B, E J, Gong J, et al. Multidisciplinary design optimization of the diesel particulate filter in the composite regeneration process. *Appl Energy*. 2016; 181: 14–28.
- [32] Bai S, Tang J, Wang G, et al. Soot loading estimation model and passive regeneration characteristics of DPF system for heavy-duty engine. *Appl Therm Eng* 2016;100:1292–8.
- [33] Bai S, Chen G, Sun Q, et al. Influence of active control strategies on exhaust thermal management for diesel particulate filter active regeneration. *Appl Therm Eng* 2017; 119:297–303.
- [34] Huq R, Anwar S. Development of a soot load sensor using electrical capacitance imaging. *J Dyn Syst Meas Contr* 2015;137(11):111009.
- [35] Zhang B, Zuo H, Huang Z, et al. Endpoint forecast of different diesel-biodiesel soot filtration process in diesel particulate filters considering ash deposition. *Fuel* 2020; 272:117678.
- [36] Huang T, Hu G, Guo F, et al. Investigation of a model-based approach to estimating soot loading amount in catalyzed diesel particulate filters. *SAE Int J Engines* 2019; 12(5):567–77.
- [37] Feulner M, Seufert F, Müller A, et al. Influencing parameters on the microwave-based soot load determination of diesel particulate filters. *Top Catal* 2017;60(3): 374–80.
- [38] Feulner M, Hagen G, Hottner K, et al. Comparative study of different methods for soot sensing and filter monitoring in diesel exhausts. *Sensors*. 2017;14(1):400–11.
- [39] Zhang J, Wong VW, Shuai S, et al. Quantitative estimation of the impact of ash accumulation on diesel particulate filter related fuel penalty for a typical modern on-road heavy-duty diesel engine. *Appl Energy* 2018;229:1010–23.

- [40] Meng Z, Chen C, Li J, et al. Particle emission characteristics of DPF regeneration from DPF regeneration bench and diesel engine bench measurements. *Fuel* 2020; 262:116589.
- [41] Chen K, Martirosyan KS, Luss D. Temperature gradients within a soot layer during DPF regeneration. *Chem Eng Sci* 2011;66(13):2968–73.
- [42] Palma V, Ciambelli P, Meloni E, et al. Catalytic DPF microwave assisted active regeneration. *Fuel* 2015;140:50–61.
- [43] Trandafilović LV, Mihai O, Woo J, et al. A kinetic model for SCR coated particulate filters—Effect of ammonia-soot interactions. *Appl Catal B* 2019;241:66–80.
- [44] Pérez VR, Bueno-López A. Catalytic regeneration of diesel particulate filters: Comparison of Pt and CePr active phases. *Chem Eng J* 2015;279:79–85.
- [45] Rothe D, Knauer M, Emmerling G, et al. Emissions during active regeneration of a diesel particulate filter on a heavy duty diesel engine: Stationary tests. *J Aerosol Sci* 2015;90:14–25.
- [46] Liu B, Sun P, Aggarwal SK, et al. An experimental-computational study of DPF soot capture and heat regeneration. *Int J Green Energy* 2020;17(4):301–8.
- [47] Serrano JR, Arnau FJ, Piqueras P, et al. Packed bed of spherical particles approach for pressure drop prediction in wall-flow DPFs (diesel particulate filters) under soot loading conditions. *Energy*. 2013;58:644–54.
- [48] Václavík M, Plachá M, Kočí P, et al. Structure characterisation of catalytic particulate filters for automotive exhaust gas aftertreatment. *Mater Charact* 2017; 134:311–8.
- [49] Lee JM, Sung NW, Cho GB, et al. Performance of radial-type metal foam diesel particulate filters. *Int J Automot Technol* 2010;11(3):307–16.
- [50] Tan P, Cao C, Hu Z, et al. Modeling of soot fragmentation that proceeds in a catalyzed diesel particulate filter of a diesel engine. *Chem Eng J* 2019;375:122110.
- [51] Kladopoulou EA, Yang SL, Johnson JH, et al. A study describing the performance of diesel particulate filters during loading and regeneration—A lumped parameter model for control applications. *SAE Trans* 2003;112(4):647–68.
- [52] Zhang B, Gong J, E J, et al. Failure recognition of the diesel particulate filter based on catastrophe theory. *Canad J Chem Eng* 2016; 94(3): 596–602.
- [53] Payri F, Broatch A, Serrano JR, et al. Experimental–theoretical methodology for determination of inertial pressure drop distribution and pore structure properties in wall-flow diesel particulate filters (DPFs). *Energy*. 2011;36(12):6731–44.